The Astrophysical Journal, 933:140 (6pp), 2022 July 10
https://doi.org/10.3847/1538-4357/ac74b2

Global Kinetic Modeling of the Intrabinary Shock in Spider Pulsars

Jorge Cortés and Lorenzo Sironi
Department of Astronomy and Columbia Astrophysics Laboratory, Columbia University, New York, NY 10027, USA; jorgecortes@astro.columbia.edu, lsironi@astro.columbia.edu

Received 2022 March 16; revised 2022 May 17; accepted 2022 May 28; published 2022 July 11

Abstract

Spider pulsars are compact binary systems composed of a millisecond pulsar and a low-mass companion. The relativistic magnetically dominated pulsar wind impacts onto the companion, ablating it and slowly consuming its atmosphere. The interaction forms an intrabinary shock, a proposed site of particle acceleration. We perform global fully kinetic particle-in-cell simulations of the intrabinary shock, assuming that the pulsar wind consists of plane-parallel stripes of alternating polarity and that the shock wraps around the companion. We find that particles are efficiently accelerated via shock-driven reconnection. We extract first-principles synchrotron spectra and light curves, which are in good agreement with X-ray observations: (1) the synchrotron spectrum is nearly flat, $F_\nu \propto$ const; (2) when the pulsar spin axis is nearly aligned with the orbital angular momentum, the light curve displays two peaks, just before and after the pulsar eclipse (pulsar superior conjunction), separated in phase by $\sim$0.8 rad; (3) the peak flux exceeds the one at the inferior conjunction by a factor of 10.

Unified Astronomy Thesaurus concepts: Pulsars (1306); Non-thermal radiation sources (1119); Shocks (2086); High energy astrophysics (739)

1. Introduction

Millisecond pulsars (MSPs) are the product of a *recycling process* that leads to their millisecond spin periods through mass accretion from a binary companion (Alpar et al. 1982). MSPs differ from *normal* pulsars by having weaker surface magnetic fields ($B_P \sim 10^8$–10^9 G), faster spin periods ($P \sim 10^{-3}$ s), smaller spin-down rates ($\dot{P} \sim 10^{-20}$ s s^{-1}), and a higher probability of being in a binary system (Manchester 2017). An interesting subclass of MSPs are the so-called spider pulsars, the redbacks (RBs) and black widows (BWs). RBs and BWs are in tight binary orbits (orbital period $P_{\rm orb} \lesssim 1$ day; orbital separation $a \sim 10^{11}$ cm) and possess either a nondegenerate companion with mass of $\sim 0.1-0.5\,M_\odot$ (for RBs) or a degenerate companion with mass of $\sim 0.01-0.05\,M_\odot$ (for BWs). In these systems, the pulsar possesses a spin-down luminosity of $\dot{E}_{\rm SD} \sim 10^{34}-10^{35}$ erg s^{-1}, emanating an intense relativistic wind. When impacting onto the companion star, the wind exacerbates ablation and mass loss of the companion (Phinney et al. 1988; Ginzburg & Quataert 2020), which is then *devoured* by the pulsar wind—hence, the evocative name of these systems.

The MSP relativistic wind consists of toroidal stripes of opposite magnetic field polarity, separated by current sheets of hot plasma (Bogovalov 1999). For obliquely rotating pulsars, this is the configuration expected around the equatorial plane of the wind, where the sign of the toroidal field alternates with the pulsar period (Pétri & Lyubarsky 2007). The wind terminates in a strong shock, where the ram pressure of the pulsar wind is balanced by the companion wind or its magnetosphere. The intrabinary shock may be an efficient site of particle acceleration (Harding & Gaisser 1990; Arons & Tavani 1993), which would then explain why X-ray light curves of spider pulsars are often modulated on the orbital period (e.g., Bogdanov et al. 2005, 2011, 2021; Huang et al. 2012; Roberts et al. 2014, 2015). The observed X-ray flux, which originates from synchrotron emission of relativistic electrons and positrons at the intrabinary shock, peaks just before and after the pulsar eclipse, which has been attributed to Doppler boosting effects caused by the post-shock flow (Romani & Sanchez 2016; Sanchez & Romani 2017; Wadiasingh et al. 2017, 2018; Kandel et al. 2019; van der Merwe et al. 2020). The X-ray spectrum is markedly nonthermal, and has flat photon indices $\Gamma_{\rm X} \approx 1-1.5$ (Roberts et al. 2015) that imply rather hard underlying electron distributions with a slope of $p = -d \log N/d \log\gamma = 2\Gamma_{\rm X} - 1 \approx 1-2$.

Relativistic hydrodynamic and magnetohydrodynamic (MHD) calculations (Bogovalov et al. 2008, 2012, 2019; Bosch-Ramon et al. 2012, 2015; Lamberts et al. 2013; Huber et al. 2021) allow to determine the overall morphology and dynamics of the system. Yet, they cannot probe the properties of the nonthermal particles responsible for the emission. In this paper, we present the first global kinetic simulations of the intrabinary shock in spider pulsars, assuming that the shock wraps around the companion star. We employ large-scale particle-in-cell (PIC) simulations, which allow to capture at the same time the global shock morphology and the microphysics of particle acceleration. We extract first-principles synchrotron spectra and light curves, and show that they are in good agreement with X-ray observations.

2. Length Scales in Spider Pulsars

The pulsar emits a relativistic magnetically dominated wind composed of stripes of alternating field polarity. Decay of the Poynting-flux-dominated stripes occurs at a radius of $R_{\rm diss} \sim 10^2$–$10^4\,R_{\rm LC}$, where $R_{\rm LC} = c/\Omega = 2\pi cP$ is the pulsar light cylinder radius (Cerutti & Philippov 2017; Cerutti et al. 2020). For the Crab, the termination shock is at $R_{\rm TS} \sim 10^9\,R_{\rm LC} \gg R_{\rm diss}$. In contrast, in spider pulsars the intrabinary shock is at $R_{\rm TS} \sim a \sim 10^{10}-10^{11}$ cm, corresponding to $R_{\rm TS} \sim 10^2-10^4\,R_{\rm LC}$ for the typical light cylinder radii of

MSPs ($R_{\rm LC} \simeq 3 \times 10^7\,(\Omega/10^3\,{\rm s}^{-1})^{-1}$ cm). It follows that the pulsar wind arrives at the intrabinary shock still in the form of magnetically dominated stripes. The compression of the flow at the shock can drive stripe annihilation via shock-driven magnetic reconnection, resulting in efficient particle acceleration (Sironi & Spitkovsky 2011; Lu et al. 2021).

We now characterize the hierarchy of length scales in spider pulsars. We consider systems in which the pulsar wind is more powerful than the companion wind, so the shock wraps around the companion star, as inferred, e.g., for the original BW PSR B1957+20. The radius of curvature of the shock $R_{\rm curv}$ is then comparable to the size $R_* \sim 10^{10}$ cm of the companion star (Burrows et al. 1993). Since the distance between the pulsar and the shock is $R_{\rm TS} \sim a \gtrsim R_{\rm curv}$, we assume for simplicity that the pulsar wind can be modeled as a sequence of plane-parallel stripes. The ratio of shock curvature radius to the stripe wavelength $\lambda = 2\pi R_{\rm LC}$ is

$$\frac{R_{\rm curv}}{\lambda} \sim 5 \times 10^1 \left(\frac{R_{\rm curv}}{10^{10}\,{\rm cm}}\right)\left(\frac{\Omega}{10^3\,{\rm s}^{-1}}\right). \tag{1}$$

The ratio of stripe wavelength to the typical post-shock Larmor radius $r_{\rm L,hot}$ is (Sironi & Spitkovsky 2011)

$$\frac{\lambda}{r_{\rm L,hot}} \sim 4\pi\kappa \frac{R_{\rm LC}}{R_{\rm TS}} \sim 3 \times 10^1 \left(\frac{\kappa}{10^4}\right) \times \left(\frac{10^{11}\,{\rm cm}}{R_{\rm TS}}\right)\left(\frac{10^3\,{\rm s}^{-1}}{\Omega}\right), \tag{2}$$

assuming a wind multiplicity (Goldreich & Julian 1969) of $\kappa \sim 10^4$ (Timokhin & Arons 2013; Timokhin & Harding 2015; Philippov et al. 2020). Local PIC simulations of shock-driven reconnection at the termination shock of striped winds have demonstrated that for $\lambda / r_{\rm L,hot} \gg 1$ the particle spectrum approaches a broad power-law tail of index $1 < p < 2$ (Sironi & Spitkovsky 2011), as required to explain the X-ray spectra of spider pulsars.

3. Simulation Setup

We use the 3D electromagnetic PIC code TRISTAN-MP (Buneman 1993; Spitkovsky 2005). We employ a 2D spatial domain in the $x-y$ plane, but we track all three components of velocity and electromagnetic fields. The magnetically dominated electron-positron pulsar wind propagates along $-\hat{x}$. It is injected from a moving boundary that starts just to the right of the companion and moves along $+\hat{x}$ at the speed of light c. This strategy allows to save memory and computing time, while retaining all the regions that are causally connected with the initial setup of the system (Sironi & Spitkovsky 2011; Sironi et al. 2013). An absorbing layer for particles and fields is placed at $x = 0$ (leftmost side of the domain). Periodic boundaries are used along the y direction. The pulsar wind magnetic field is initialized as

$$B_y(x,\,t) = B_0 \tanh\left\{\frac{1}{\Delta}\left[\alpha + \cos\left(\frac{2\pi(x + \beta_0 ct)}{\lambda}\right)\right]\right\}, \tag{3}$$

where $\beta_0 = (1 - 1/\gamma_0^2)^{1/2}$ is the wind velocity and γ_0 the bulk Lorentz factor. We present results for $\gamma_0 = 3$, but we have verified that a choice of $\gamma_0 = 10$ leads to the same conclusions, apart from an overall shift in the energy scale (see also Sironi & Spitkovsky 2011). The field direction flips across current sheets of thickness $\sim\Delta\lambda$. The field strength B_0 is parameterized via the magnetization $\sigma \equiv B_0^2 / 4\pi\,\gamma_0 m n_0 c^2 = 10$ (i.e., the ratio of Poynting to kinetic energy flux). Here, m is the electron (or positron) mass and n_0 the density of particles in the *cold wind* (i.e., the region outside of current sheets, which instead have a peak density of $4\,n_0$). Finally, α is a measure of the magnetic field averaged over one wavelength, such that $\langle B_y \rangle_\lambda / B_0 = \alpha/(2 - |\alpha|)$. A value of $\alpha = 0$—or equivalently, *positive* and *negative* stripes of comparable width—indicates the equatorial plane of the pulsar, whereas $|\alpha|$ increases when moving away from the midplane (Sironi & Spitkovsky 2011). For BWs, the spin axis of the pulsar is believed to be well aligned with the orbital angular momentum (Roberts 2013), so we will only explore small values of α, from 0 up to 0.3.

The relativistic skin depth in the cold wind $c/\omega_{\rm p} \equiv (\gamma_0 mc^2/4\pi e^2 n_0)^{1/2}$ is resolved with 10 cells, so the pre-shock Larmor radius $r_{\rm L} \equiv \gamma_0 mc^2/eB_0 = (c/\omega_{\rm p})/\sqrt{\sigma}$ is resolved with three cells. The post-shock Larmor radius, assuming complete field dissipation, is defined as $r_{\rm L,hot} = \sigma r_{\rm L}$. The numerical speed of light is 0.45 cells/timestep. Within the cold wind, each computational cell is initialized with two pairs of cold ($kT/mc^2 = 10^{-4}$) electrons and positrons, but we have checked that higher numbers of particles per cell lead to the same results. The temperature in the overdense current sheets is set by pressure balance.

Our computational domain is $4800\,c/\omega_{\rm p}$ wide (in the y direction), or equivalently 48,000 cells wide. The center of the companion is placed at $(x,\;y) = (1500,\;2400)\,c/\omega_{\rm p}$, with a companion radius of $R_* = 70\,c/\omega_{\rm p}$. The companion surface (a cylinder, for our 2D geometry) is a conducting boundary for fields and a reflecting boundary for particles. The value for R_* is chosen such that the companion wind (see below) is stopped by the pulsar wind at $R_{\rm curv} \simeq 200\,c/\omega_{\rm p}$, which then gives the characteristic shock curvature radius. The large width of our domain in the y direction is required such that the shock wraps around the companion until the $x = 0$ open boundary, i.e., the shock surface does not cross the periodic y boundaries. We set the stripe wavelength to be $\lambda = 100\,c/\omega_{\rm p}$. It follows that $R_{\rm curv}/\lambda \simeq 2$ and $\lambda / r_{\rm L,hot} \simeq 30$, i.e., similar values (within one order of magnitude) as inferred in spider pulsar systems. Even larger values of $R_{\rm curv}/\lambda$ will be discussed in an upcoming work.

In our setup, the pulsar wind is stopped by a companion wind launched isotropically from its surface. We do not aim to reproduce the realistic properties of the companion wind. In fact, it would be numerically unfeasible to resolve the plasma scales in a dense non-relativistic companion wind, and yet perform global simulations of the system. Given that our focus is on pulsar wind particles, their acceleration and emission, the companion wind will merely serve to halt the pulsar wind. We initialize a companion wind with realistic values of the radial momentum flux, but with artificially smaller particle density (and so, artificially higher wind velocity) to make the problem computationally tractable. The momentum flux density of the companion wind at the companion surface is two times larger than the momentum flux of the pulsar wind. We have tested that different choices for the companion wind density (at fixed momentum flux) lead to identical results for the structure, dynamics, and particle acceleration properties of the pulsar wind termination shock. In the remainder of this work we will only consider acceleration and emission of pulsar wind

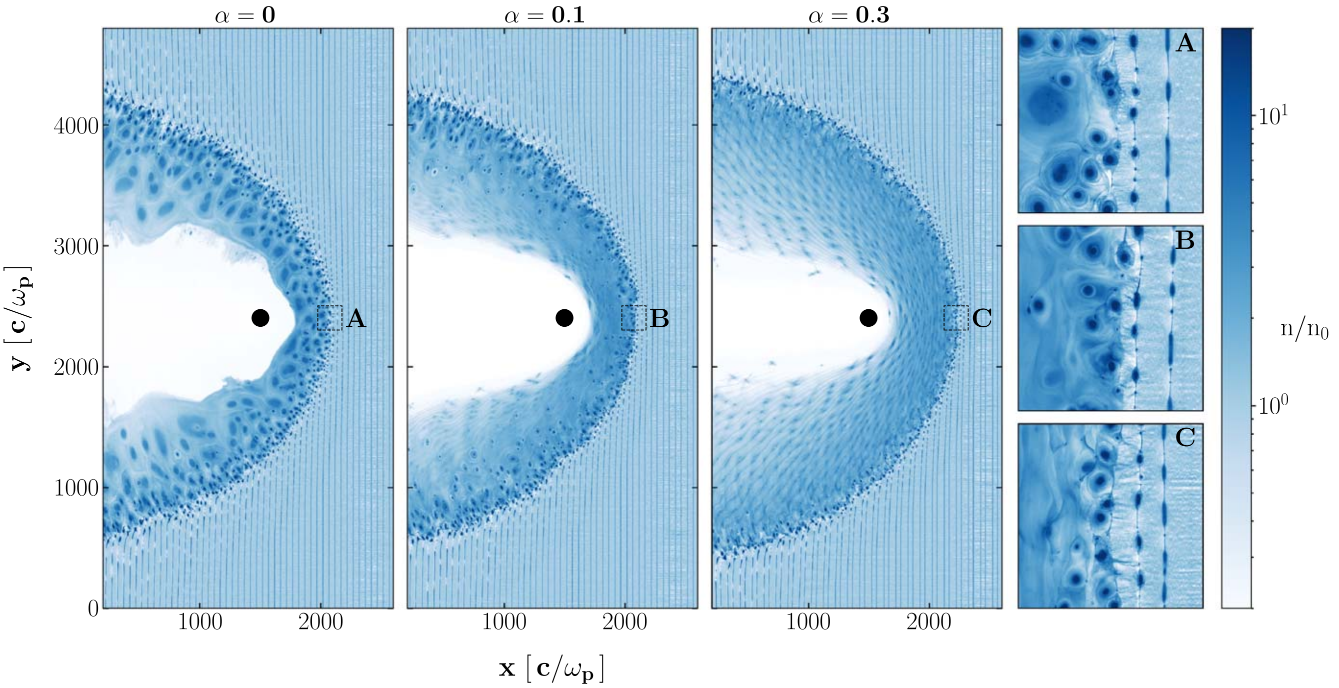

Figure 1. 2D plots of the number density of pulsar wind particles, in units of n_0, for $\alpha = 0$, 0.1, and 0.3 (left to right panels). The plots refer to $\omega_p t = 3510$. The black filled circle represents the companion star. Insets A, B, and C—marked in the main panels by a square box delimited by black dashed lines—provide a zoom-in view highlighting the formation of magnetic islands/plasmoids due to shock-driven reconnection.

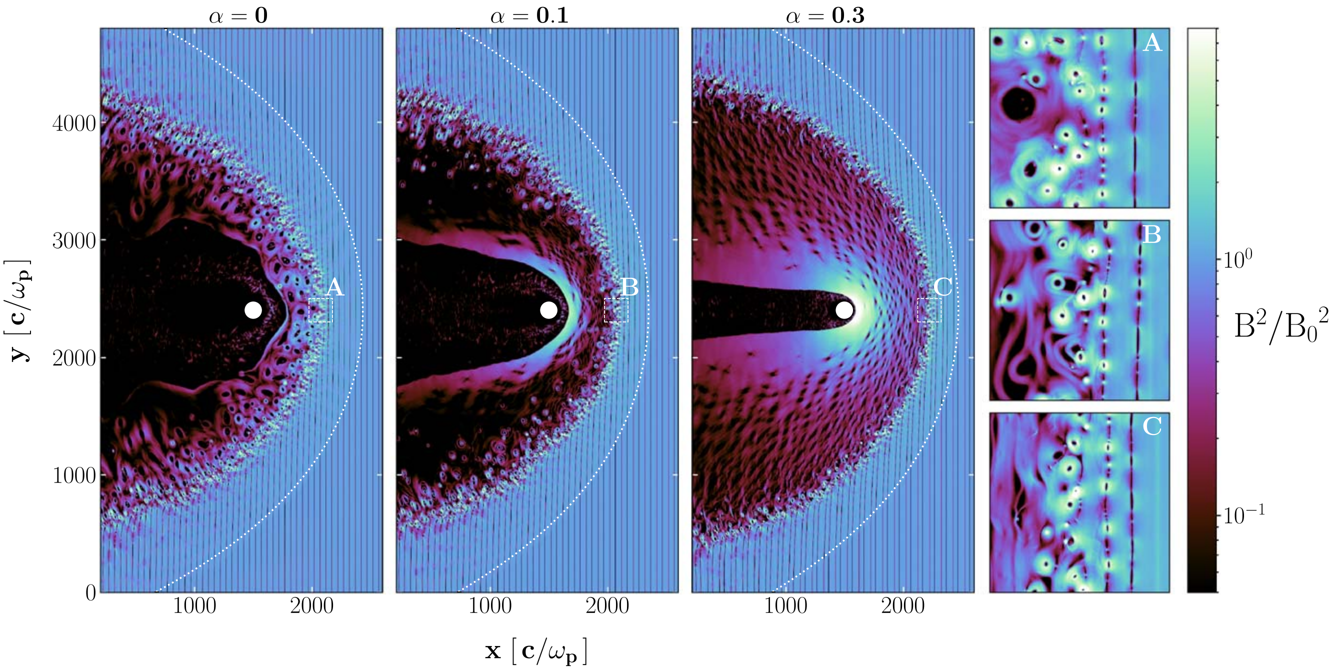

Figure 2. 2D plots of the magnetic energy density, in units of the upstream value $B_0^2/8\pi$, for $\alpha = 0$, 0.1, and 0.3 (left to right). The plots refer to $\omega_p\, t = 3510$. The white filled circle represents the companion star. Insets A, B, and C—marked in the main panels by a square box delimited by white dashed lines—are as in Figure 1. Dotted white lines indicate the fast MHD shock.

particles; therefore, by *wind* we will refer to the pulsar wind, unless otherwise specified.

4. Flow Dynamics

Figures 1 and 2 show the number density of pulsar wind particles (Figure 1) and the magnetic energy density (Figure 2) on the global scale of the intrabinary shock. From left to right, we show $\alpha = 0$, 0.1, and 0.3. All panels refer to $\omega_p t = 3510$, when for $\alpha = 0$ the system has approached a quasi-steady state. The interaction between the pulsar wind and the companion wind is expected to generate two shocks (a reverse shock into the companion wind, and a forward shock into the pulsar wind) and a contact discontinuity. The reverse shock is visible only for $\alpha = 0$ and 0.1 in Figure 2, as an arc of small-scale magnetic fields just to the right of the companion. In our setup, the companion wind is unmagnetized, and the reverse shock is mediated by the filamentation (or, Weibel) instability, which creates intense small-scale fields (e.g., Sironi et al. 2013). The contact discontinuity is clearly seen, as the surface wrapping around the companion that delimits the white region in Figure 1 and the dark/black region in Figure 2. Both pulsar wind particles and strong fields are primarily confined to the right of the contact discontinuity.

The forward shock that stops the pulsar wind is the location where the ordered plane-parallel structure of the pre-shock wind transitions toward a more disordered, turbulent medium that flows around the companion and ultimately exits the left boundary. As described in local PIC simulations of relativistic striped winds (Sironi & Spitkovsky 2011; Lu et al. 2021), at the shock the flow compresses and the alternating fields annihilate via shock-driven reconnection. In fact, the overdense, magnetized, quasi-circular blobs seen in the rightmost columns of both figures are the characteristic magnetic islands/plasmoids produced by reconnection.

More precisely, reconnection starts ahead of the main shock, at a fast MHD shock (dotted white lines in Figure 2) that propagates into the pre-shock striped flow, compressing the incoming current sheets and initiating reconnection. When reconnection islands grow so big to occupy the entire region between neighboring current sheets, the striped structure is erased, and the main shock forms (at the boundary where B^2/B_0^2 turns from cyan to purple in Figure 2). For $\alpha \leqslant 0.3$, the average post-shock particle energy is larger than in the pre-shock wind by a factor of $\simeq\sigma$. Equivalently, most of the pre-shock field energy has been transferred to the particles.

For $\alpha \neq 0$, the stripe-averaged field $\langle B_y \rangle_\lambda / B_0 = \alpha/(2 - |\alpha|)$ does not annihilate, and its field lines secularly accumulate, for our 2D geometry, in front of the companion star (see Figure 2 for $\alpha = 0.1$ and 0.3).[1] This accumulation of magnetic energy/pressure is expected to be alleviated in 3D, as the field lines can pass above/below the spherical companion (in contrast to the cylindrical companion in 2D).

The plasmoids are primarily concentrated near the shock. For $\alpha = 0$, it is apparent that they merge with each other and grow in scale while flowing away from the shock, with the largest plasmoids having a size that is comparable to global scales (e.g., to the shock curvature radius).

5. Particle Acceleration and Emission

PIC simulations provide a first-principles assessment of the physics of particle acceleration and the properties of the resulting emission. We compute the synchrotron emission contributed by the post-shock pulsar wind particles.[2] In Figure 3(a), the top three curves show the angle-integrated synchrotron spectra for the three values of α explored in this work (see legend). The three lines with lower normalization, instead, are the spectra measured at the orbital phase $|\phi| = \pi/8$ corresponding to the two light-curve peaks for $\alpha = 0$, as we show in Figure 4 (*peak-phase* spectra). Phase-resolved spectra are computed as follows. We consider a set of $N_{\rm los} = 32$ lines of sight, all lying in the simulation plane (equivalently, the orbital plane) and equally spaced in angle between $-\pi$ and π. We take $\phi = 0$ at superior conjunction (when the pulsar is eclipsed by the companion), and $\phi = \pm\pi$ at inferior conjunction. For each line of sight, the synchrotron emission is contributed by those particles whose velocity lies within an angle $\pi/N_{\rm los}$ from the line of sight. For each line of sight, we exclude the contribution from the spatial regions eclipsed by the companion (but we assume its wind to be optically thin).

All spectra in Figure 3(a) display the usual $\nu F_\nu \propto \nu^{4/3}$ at low frequencies, with a transition to $\nu F_\nu \propto \nu^{0.8}$ in the range $\chi = \omega/\omega_{\rm c} \sim 10^{-2}$–$10^1$. A spectrum $\nu F_\nu \propto \nu^{0.8}$ is in good agreement with X-ray observations, since it corresponds to a photon spectral index $\Gamma_{\rm X} \simeq 1.2$. Here, the characteristic synchrotron frequency $\omega_{\rm c} = (\gamma_0 \sigma)^2 e B_0/mc$ is calculated for the average post-shock Lorentz factor $\gamma = \gamma_0 \sigma$ assuming efficient dissipation of the alternating stripes. Since $\sigma = 10$ in our simulations, a value of $\chi \sim 10^{-2}$ then corresponds to the characteristic emission frequency of particles with $\gamma = \gamma_0$.

Further insight is provided by the downstream energy spectra of pulsar wind particles, shown in Figure 3(b) There, we multiply the particle count $dN/d\log(\gamma - 1)$ by an additional factor of $(\gamma^2 - 1)$, proportional to the synchrotron power per particle. Between $\gamma = \gamma_0 = 3$ and $\gamma = \gamma_0 \sigma = 30$, the particle spectrum can be modeled as a hard power law $dN/d\gamma \propto \gamma^{-p}$ with slope $p \simeq 1.4$. Local simulations of relativistic striped winds (Sironi & Spitkovsky 2011) have shown that shock-driven reconnection leads, in the limit $\lambda/r_{\rm L,hot} \gg 1$, to hard power-law distributions, with a slope consistent with what we measure here. It follows that the synchrotron spectral range between $\chi \sim 10^{-2}$ and $\chi \sim 10^1$ is contributed by particles accelerated via shock-driven reconnection. For $p \simeq 1.4$, the resulting synchrotron spectrum will be $\nu F_\nu \propto \nu^{(3-p)/2} = \nu^{0.8}$, as indeed can be observed in Figure 3(a). The three α cases all exhibit the same spectral slope between $\chi \sim 10^{-2}$ and $\chi \sim 10^1$. Their difference at higher ($\chi \gtrsim 10^2$) frequencies mirrors the trend in the corresponding particle energy spectra, and it is due to differences in the acceleration physics of particles with $\gamma \gg \gamma_0 \sigma$, as we will discuss in an upcoming work.

Phase-resolved light curves are shown in Figure 4, for two values of χ within the $\nu F_\nu \propto \nu^{0.8}$ spectral range: $\chi = 1$ (top three lines) and $\chi = 10^{-1}$ (bottom three lines). All curves are normalized to the peak of the $\alpha = 0.3$ light curve at $\chi = 1$. The two sets of lines display similar properties (they differ, at zeroth order, only by an overall normalization factor): the $\alpha = 0.3$ light curve (cyan dashed) is strongly peaked at superior conjunction ($\phi = 0$, when the pulsar is eclipsed by the companion); the peak is shallower for $\alpha = 0.1$ (black dotted–dashed); interestingly, for $\alpha = 0$ (red solid) the light curve peaks at $\phi \simeq \pm\pi/8$, i.e., just before and after superior conjunction. For $\alpha = 0$, the two peaks are separated by $\simeq 0.8$ rad (equivalently, ~0.13 in normalized phase), and the flux at $\phi = 0$ drops by ~10% below the peak flux. The flux at inferior conjunction ($\phi = \pm\pi$) is nearly a factor of 10 lower than the peak. All these properties hold throughout the spectral range $\chi = 10^{-2}$–10^1 where $\nu F_\nu \propto \nu^{0.8}$, and are in good agreement with X-ray data (e.g., Bogdanov et al. 2005, 2011, 2021; Huang et al. 2012; Roberts et al. 2014, 2015).

6. Summary and Discussion

We have performed global fully kinetic PIC simulations of the intrabinary shock in spider pulsars. We assumed that the pulsar wind consists of plane-parallel stripes of alternating polarity and that the shock wraps around the companion star.

---

[1] The larger magnetic pressure accumulating around the companion may also be the reason why the contact discontinuity wraps more tightly around the companion for higher α.

[2] Radiative cooling losses are not accounted for in the particle equation of motion, i.e., we assume a slow-cooling regime.

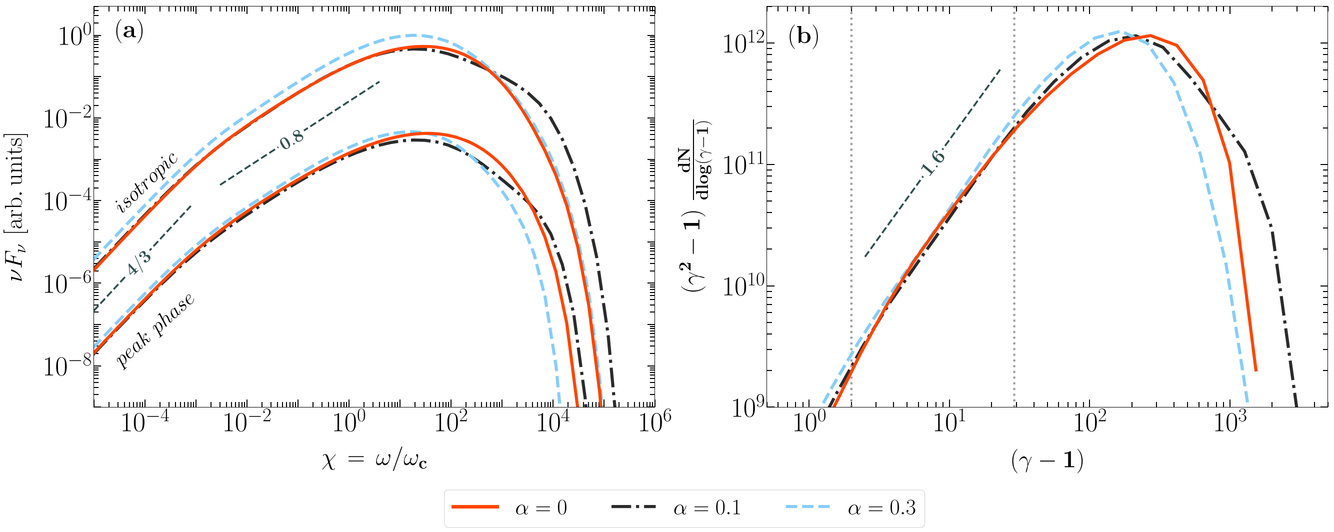

Figure 3. (a) Synchrotron spectra νF_ν for $\alpha = 0$ (red solid) 0.1 (black dotted–dashed) and 0.3 (cyan dashed) at $\omega_p\, t = 3510$, the same time as in Figure 1. We define $\chi = \omega/\omega_c$ where the characteristic synchrotron frequency $\omega_c = (\gamma_0\sigma)^2 eB_0/mc$ is calculated for the average post-shock Lorentz factor $\gamma = \gamma_0\sigma$. We show both angle-integrated spectra (top series of lines) and spectra measured at the orbital phase $|\phi| = \pi/8$ corresponding to the two light-curve peaks for $\alpha = 0$ (peak-phase spectra; bottom series). (b) Particle energy spectra for the different α cases, with the same color and line style coding as in (a). We multiply the particle count $dN/d\log(\gamma-1)$ by an additional factor of $(\gamma^2 - 1)$, proportional to the synchrotron power per particle. Vertical dotted lines are for $\gamma = \gamma_0$ and $\gamma = \gamma_0\sigma$.

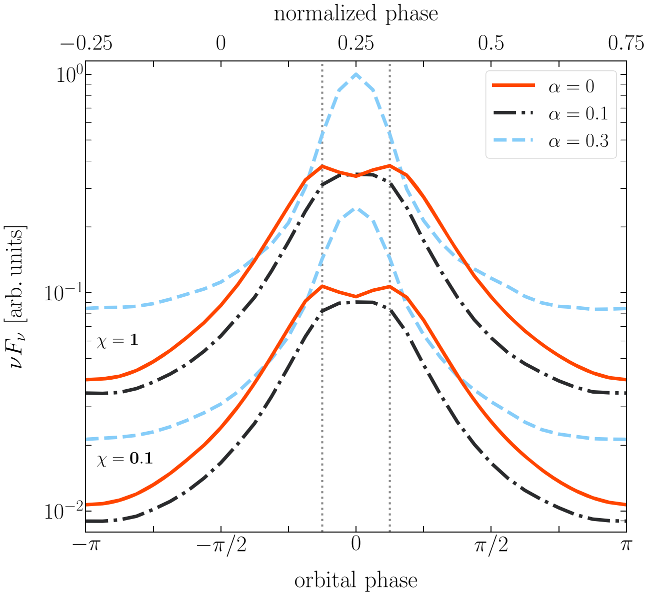

Figure 4. Synchrotron light curves for $\alpha = 0$ (red solid), 0.1 (black dotted–dashed), and 0.3 (cyan dashed) at $\omega_p t = 3510$, as a function of orbital phase ϕ (bottom axis). We choose $\phi = 0$ to correspond to superior conjunction (when the pulsar is eclipsed), while $\phi = \pm\pi$ to inferior conjunction. The top axis is the normalized phase, with 0.25 at the pulsar superior conjunction, as typical for X-ray observations. The light curves are shown for both $\chi = 0.1$ (bottom lines) and 1 (top lines), where $\chi = \omega/\omega_c$. Gray dotted lines at $|\phi| = \pi/8$ indicate the location of the two peaks for the $\alpha = 0$ case.

We find that pulsar wind particles are efficiently accelerated at the shock via shock-driven reconnection. We extract first-principles synchrotron spectra and light curves and we find that (1) the synchrotron spectrum is nearly flat ($F_\nu \propto$ const); (2) when the pulsar spin axis is nearly aligned with the orbital angular momentum, the light curve displays two peaks, just before and after the pulsar eclipse (superior conjunction of the pulsar), separated in phase by ∼0.8 rad (equivalently, ∼0.13 in normalized phase); this likely comes from Doppler boosting in the post-shock flow, as suggested by Romani & Sanchez (2016) and Wadiasingh et al. (2017); (3) the peak flux exceeds the one at inferior conjunction by a factor of 10.

Our simulations reproduce, within one order of magnitude, the hierarchy of length scales expected in spider pulsars. However, we employ smaller values of γ_0 and σ than expected in pulsar winds. While we have tested that a change in γ_0 only leads to a shift in the overall energy scale, upcoming simulations with larger σ will be needed to clarify whether $\sigma = 10$ is already in the asymptotic $\sigma \gg 1$ limit, as local PIC simulations suggest (Sironi & Spitkovsky 2011). One may wonder, within our model, whether realistic values of $\gamma_0\sigma$ are such that the resulting emission at $\sim\omega_c$ falls in the X-ray band. Conservation of energy along the pulsar wind streamlines implies that $\gamma_0\,(1+\sigma)\,\kappa = \omega_{LC}/2\,\Omega$, where $\omega_{LC} = eB_{LC}/mc$ is the cyclotron frequency at the light cylinder radius. We extrapolate the field from the pulsar surface to the light cylinder radius with a dipolar scaling, $B_{LC} \sim B_P\ (R_{NS}/R_{LC})^3$ (here, $R_{NS} \sim 10$ km is the neutron star radius). We assume that the post-shock field is of the same order as the pre-shock field $B_0 \sim B_{LC}\ (R_{LC}/R_{TS})$. The characteristic synchrotron photon energy will be

$$\hbar\omega_c = \hbar\,(\gamma_0\sigma)^2 \frac{eB_0}{mc} \simeq 0.2\left(\frac{10^4}{\kappa}\right)^2\left(\frac{10^{11}\,\mathrm{cm}}{R_{TS}}\right)\left(\frac{B_P}{10^9\,\mathrm{G}}\right)^3\left(\frac{\Omega}{10^3\,\mathrm{s}^{-1}}\right)^6 \mathrm{keV}. \quad (4)$$

The peaks of our synchrotron spectra are located at $\sim 20\hbar\omega_c$. Thus, for realistic parameters, our conclusions on light-curve shape and spectral hardness below the peak can be promptly applied to X-ray observations. We also remark that the synchrotron peak frequency, via Equation 4, may provide important constraints on the multiplicity κ of pulsar winds, if both the pulsar period P and its derivative $\dot{P}$ (and so, also $B_P \propto \sqrt{P\dot{P}}$) are measured.

We conclude with a few caveats. First, we have employed 2D simulations, and we defer to future work an assessment of

3D effects (e.g., for cases with $\alpha \neq 0$, in 2D field lines artificially accumulate ahead of the companion). Second, we have neglected the orbital motion of the system, which has been invoked to explain asymmetries in the light curve, with the two peaks having different heights (Kandel et al. 2021). Third, we have ignored radiative cooling losses in the particle equation of motion. Depending on parameters, the post-shock flow may be slow- or fast-cooling (Wadiasingh et al. 2017), so our results are applicable only to the slow-cooling cases. Finally, it will be desirable to extrapolate our results to larger values of $R_{\rm curv}/\lambda$, as we will do in an upcoming work.

J.C. thanks the LSSTC Data Science Fellowship Program, which is funded by LSSTC, NSF Cybertraining Grant 1829740, the Brinson Foundation, and the Moore Foundation; J.C.'s participation in the program has benefited this work. L.S. acknowledges support from the Cottrell Scholars Award, NASA 80NSSC20K1556, NSF PHY-1903412, DoE DE-SC0021254, and NSF AST-2108201. The authors thank S. Bogdanov, V. Bosch-Ramon, A.K. Harding, B.D. Metzger, R. W. Romani, and Z. Wadiasingh for helpful and insightful comments. The authors acknowledge computing resources from Columbia University's Shared Research Computing Facility project, which is supported by NIH Research Facility Improvement Grant 1G20RR030893-01, and associated funds from the New York State Empire State Development, Division of Science Technology and Innovation (NYSTAR) Contract C090171, both awarded on 2010 April 15. Lastly, the authors thank the anonymous referee for useful comments and critiques.

ORCID iDs

Jorge Cortés https://orcid.org/0000-0001-5186-6195
Lorenzo Sironi https://orcid.org/0000-0002-1227-2754

References

Alpar, M. A., Cheng, A. F., Ruderman, M. A., & Shaham, J. 1982, Natur, 300, 728
Arons, J., & Tavani, M. 1993, ApJ, 403, 249
Bogdanov, S., Archibald, A. M., Hessels, J. W. T., et al. 2011, ApJ, 742, 97
Bogdanov, S., Bahramian, A., Heinke, C. O., et al. 2021, ApJ, 912, 124
Bogdanov, S., Grindlay, J. E., & van den Berg, M. 2005, ApJ, 630, 1029
Bogovalov, S. V. 1999, A&A, 349, 1017
Bogovalov, S. V., Khangulyan, D., Koldoba, A., Ustyugova, G. V., & Aharonian, F. 2019, MNRAS, 490, 3601
Bogovalov, S. V., Khangulyan, D. V., Koldoba, A. V., Ustyugova, G. V., & Aharonian, F. A. 2008, MNRAS, 387, 63
Bogovalov, S. V., Khangulyan, D., Koldoba, A. V., Ustyugova, G. V., & Aharonian, F. A. 2012, MNRAS, 419, 3426
Bosch-Ramon, V., Barkov, M. V., Khangulyan, D., & Perucho, M. 2012, A&A, 544, A59
Bosch-Ramon, V., Barkov, M. V., & Perucho, M. 2015, A&A, 577, A89
Buneman, O. 1993, Computer Space Plasma Physics (Tokyo: Terra Scientific), 67
Burrows, A., Hubbard, W. B., Saumon, D., & Lunine, J. I. 1993, ApJ, 406, 158
Cerutti, B., & Philippov, A. A. 2017, A&A, 607, A134
Cerutti, B., Philippov, A. A., & Dubus, G. 2020, A&A, 642, A204
Ginzburg, S., & Quataert, E. 2020, MNRAS, 495, 3656
Goldreich, P., & Julian, W. H. 1969, ApJ, 157, 869
Harding, A. K., & Gaisser, T. K. 1990, ApJ, 358, 561
Huang, R. H. H., Kong, A. K. H., Takata, J., et al. 2012, ApJ, 760, 92
Huber, D., Kissmann, R., Reimer, A., & Reimer, O. 2021, A&A, 646, A91
Kandel, D., Romani, R. W., & An, H. 2019, ApJ, 879, 73
Kandel, D., Romani, R. W., & An, H. 2021, ApJL, 917, L13
Lamberts, A., Fromang, S., Dubus, G., & Teyssier, R. 2013, A&A, 560, A79
Lu, Y., Guo, F., Kilian, P., et al. 2021, ApJ, 908, 147
Manchester, R. N. 2017, JApA, 38, 42
Pétri, J., & Lyubarsky, Y. 2007, A&A, 473, 683
Philippov, A., Timokhin, A., & Spitkovsky, A. 2020, PhRvL, 124, 245101
Phinney, E. S., Evans, C. R., Blandford, R. D., & Kulkarni, S. R. 1988, Natur, 333, 832
Roberts, M. S. E. 2013, in IAU Symp. 291, Neutron Stars and Pulsars: Challenges and Opportunities after 80 Years, ed. J. van Leeuwen (Cambridge: Cambridge Univ. Press), 127
Roberts, M. S. E., Mclaughlin, M. A., Gentile, P., et al. 2014, AN, 335, 313
Roberts, M. S. E., McLaughlin, M. A., Gentile, P. A., et al. 2015, arXiv:1502.07208
Romani, R. W., & Sanchez, N. 2016, ApJ, 828, 7
Sanchez, N., & Romani, R. W. 2017, ApJ, 845, 42
Sironi, L., & Spitkovsky, A. 2011, ApJ, 741, 39
Sironi, L., Spitkovsky, A., & Arons, J. 2013, ApJ, 771, 54
Spitkovsky, A. 2005, in AIP Conf. Ser. 801, Astrophysical Sources of High Energy Particles and Radiation, ed. E. R. Bulik, B. Rudak, & G. Madejski (Melville, NY: AIP), 345
Timokhin, A. N., & Arons, J. 2013, MNRAS, 429, 20
Timokhin, A. N., & Harding, A. K. 2015, ApJ, 810, 144
van der Merwe, C. J. T., Wadiasingh, Z., Venter, C., Harding, A. K., & Baring, M. G. 2020, ApJ, 904, 91
Wadiasingh, Z., Harding, A. K., Venter, C., Böttcher, M., & Baring, M. G. 2017, ApJ, 839, 80
Wadiasingh, Z., Venter, C., Harding, A. K., Böttcher, M., & Kilian, P. 2018, ApJ, 869, 120